


Simple dynamical model that leads to sputter cone formationNicholas L. Lehnerz *Department of Physics, Colorado State University, Fort Collins, Colorado 80523, USA*R. Mark Bradley *Departments of Physics and Mathematics, Colorado State University, Fort Collins, Colorado 80523, USA*

(Received 27 March 2024; accepted 9 July 2024; published 14 August 2024)

We introduce a model for sputter cone formation that includes only the angular dependence of the sputter yield and a fourth-order smoothing effect like surface diffusion. In one dimension, a sputter cone is a particular kind of shock wave that is known as an undercompressive shock. Simulations of our model show that a wide variety of initial conditions lead to the formation of sputter cones and that the opening angle of the cones does not depend on the detailed form of the initial condition. In two dimensions, a sputter cone is a higher-dimensional analog of an undercompressive shock. For two particularly simple choices of parameters, a sputter cone is a four-sided pyramid with rounded edges that is produced by the superposition of two orthogonal, one-dimensional undercompressive shocks.

DOI: [10.1103/PhysRevE.110.024802](https://doi.org/10.1103/PhysRevE.110.024802)**I. INTRODUCTION**

In a now-classic kind of experiment, the initially planar surface of a solid composed of the elemental material **B** is bombarded with a broad, normally incident noble-gas ion beam and impurity atoms of species **A** are deposited concurrently. If the sputter yield of material **A** is lower than the yield of material **B**, then, after a time, a disordered array of conical projections appears on the surface of the sample [1–8]. These so-called sputter cones are said to be “seeded” by the codeposition of atoms of species **A**. It has been argued that sputter cones form as the impurity atoms diffuse and agglomerate on the surface [1–3]. These agglomerations would have a low sputter yield, and so they would shield the underlying material from the ion flux, leading to the formation of protrusions with clusters of impurity atoms at their apexes.

Sputter cones are close to being conical away from their tips, which are rounded. In addition, the cones all seem to have very nearly the same opening angle in a given experiment. The opening angle does, however, depend on the choice of materials and on the ion species and energy. These observations have not yet been satisfactorily explained, even though the first account of sputter cone formation appeared in the literature over 80 years ago [9].

Sputter cones can also be produced in a different fashion that will be the focus of this paper [10]. In this alternate approach, atoms of atomic species **A** are not deposited during ion bombardment of the sample surface. Instead, a thin film of material **A** is first deposited on the planar surface of a sample composed of material **B**. The surface of the sample is then subjected to normal-incidence bombardment with a broad noble gas ion beam. Because the thickness of a thin film is never completely uniform, after a time, only isolated patches of material **A** remain. These patches shield the material **B** beneath them from being sputtered, and protrusions therefore

form on the surface of the substrate. In time, the isolated patches of low sputter yield material are also eroded away and only material **B** remains. Protrusions will, however, still be present on the surface. As the ion bombardment continues, the protrusions become nearly conical in form if material **B** is amorphous. If material **B** is crystalline and remains so during the ion erosion, then the protrusions are polygonal pyramids instead of cones [10].

The formation of sputter cones is fascinating, and it is not just of academic interest. Metal cones with sharp tips can be operated as cold cathodes at a low electric fields and might be useful in flat-panel displays, for example [6]. In addition, a dense array of sputter cones can greatly enhance the optical absorption of a surface and so could play a crucial role in increasing the efficiency of solar cells [11].

In this paper, we introduce and study a model that leads to sputter cone formation. In general, quite a number of physical phenomena could conceivably contribute to the formation of sputter cones, although the effect of some of these is expected to be minor. Rather than attempt to incorporate all of the different phenomena that might have an influence, we will develop a model that is as simple as possible but nevertheless contains the essential physics needed to produce sputter cones. In particular, we show that a model that includes only the angular dependence of the sputter yield and a fourth-order smoothing effect like surface diffusion produces sputter cones. We begin by studying our model in one dimension (1D). We show that a sputter cone is a particular kind of shock wave that is known as an undercompressive shock. Our numerical integrations of our equation of motion (EOM) for the solid surface show that a wide variety of initial conditions lead to the formation of sputter cones and that the morphology and the opening angle of the cones does not depend on the detailed form of the initial condition. We then show how these ideas generalize to two dimensions. In this case, a sputter cone is a

higher-dimensional analog of an undercompressive shock. For two particularly simple choices of parameters, a sputter cone is a superposition of two orthogonal 1D undercompressive shocks.

This paper is organized as follows: We develop our minimal model of sputter cone formation in Sec. II. We carry out an analytical study of our EOM in Sec. III and find exact sputter cone solutions in both one and two dimensions. We extend the model to include the effects of curvature-dependent sputtering and ion-induced mass redistribution in Sec. IV. The simulation results given in Sec. V show that for a broad range of initial conditions, the surface converges to the sputter cone solutions we found in Sec. III. Additional discussion of our results is given in Sec. VI and we conclude in Sec. VII.

II. FORMULATION OF THE PROBLEM

When two nonvolatile atomic species are present in a solid that is irradiated with a noble gas ion beam, the surface morphology and composition are coupled. It is therefore not sufficient to simply keep track of the surface morphology. Instead, coupled partial differential equations that give the time evolution of the surface height and composition are needed [12–20]. For this reason, theoretical analysis of the problem in which ion bombardment and impurity codeposition are carried out concurrently is challenging. A theory has been developed, but it applies only at early times when the surface slopes are small and mature sputter cones have not yet formed [15–20]. We therefore restrict our attention to the version of the problem in which a thin film of material **A** is initially present on the planar surface of the sample of material **B** and focus on the dynamics that occur after material **A** has been entirely removed by the ion bombardment. We also adopt the customary assumption that the implantation of noble gas ions is negligible [21]. Therefore, because we have assumed that material **B** is elemental, in effect only one atomic species is present in the target once all of the thin film of material **A** has been sputtered away. The state of the surface at the point in time when the last of material **A** has been eroded away will be the initial condition for the problem we will consider.

We adopt a continuum description of the solid surface. The z axis will be taken to be normal to the planar surface of material **B** before the ion bombardment begins and to point away from the bulk of material **B**. Let $h = h(x, y, t)$ denote the height of the surface of material **B** above the point (x, y) in the x - y plane at time t . The surface height of material **B** at the time when the last of material **A** is removed, i.e., at time $t = 0$, is $h(x, y, 0)$. We assume that $h(x, y, 0)$ is a single-valued, smooth function of x and y . The partial derivative of h with respect to x will be denoted by h_x , and h_y and h_t are defined analogously. Above the solid, the incident ion current is $\mathbf{J} = -J\hat{z}$, where J is a positive constant and \hat{z} is the unit vector that points along the positive z axis.

Material **B** may be amorphous or crystalline. If it is crystalline initially, then there are two cases to be considered. If a layer at the surface of the material is amorphized by the ion bombardment, then, after a transient, the problem is essentially the same as material **B** were amorphous in its entirety. On the other hand, if material **B** remains crystalline, then

we assume that the crystal structure has fourfold rotational symmetry about the z axis for the sake of simplicity.

Our goal is to develop a model that is as simple as possible but nevertheless contains the essential physics needed to produce sputter cones. We will therefore make a number of simplifying assumptions; these will be discussed later in this section.

For the moment, we will only take into account the effect of sputtering. The EOM for the surface is then simply

$$h_t = -\Omega JY, \quad (1)$$

where Y is the sputter yield and Ω is the atomic volume for material **B**. The sputter yield will be taken to depend only on the local angle of incidence or, equivalently, to depend only on h_x and h_y . Thus, $Y = Y(h_x, h_y)$. If material **B** is amorphous or is amorphized by the ion bombardment, then $Y(h_x, h_y)$ is invariant under all possible rotations about the z axis and so it only depends on $|\nabla h|$. If the material is crystalline, on the other hand, then $Y(h_x, h_y)$ is only fourfold rotationally invariant. In this case, $Y(h_x, h_y)$ is invariant under the transformations $h_x \rightarrow -h_x$ and $h_y \rightarrow -h_y$ and is unchanged if h_x and h_y are interchanged.

Consider the flat surface of an amorphous material and suppose that an ion beam with the angle of incidence θ is incident on it. (θ is defined to be the angle between the surface normal and the direction of ion incidence, and so $\theta = 0$ for a normally incident beam.) The sputter yield increases at first as θ is increased from zero but then passes through a maximum and begins to decrease. Therefore, if an ion beam is normally incident on a planar surface with a constant height gradient ∇h , then the sputter yield Y is an increasing function of $|\nabla h|$ for small $|\nabla h|$, but as $|\nabla h|$ is increased further, Y passes through a maximum and then starts to decrease. We will adopt a particularly simple form for $Y = Y(h_x, h_y)$ that has these attributes: We set

$$Y = Y_0 + a(\nabla h)^2 - c(\nabla h)^4, \quad (2)$$

where $Y_0 \equiv Y(0, 0)$ and a and c are positive constants. As we shall see, this form for Y has the virtue that analytical results can be obtained in certain cases.

If the material remains crystalline during the ion bombardment, then $Y(h_x, h_y)$ is only fourfold rotationally invariant. We can generalize our simple choice of Y so that this is also a possibility: We set

$$Y = Y_0 + a(\nabla h)^2 - c(\nabla h)^4 - c' h_x^2 h_y^2, \quad (3)$$

where c' is a constant. When c' is nonzero, the sputter yield is only fourfold rotationally invariant. Complete rotational invariance is recovered for $c' = 0$.

We now insert the sputter yield Y given by Eq. (3) into Eq. (1). We can simplify the resulting equation by setting $h(x, y, t) = -v_0 t + u(x, y, t)$, where $v_0 \equiv \Omega J Y_0$ is the rate that a flat surface of material **B** would recede if it were bombarded with the ion beam; $u(x, y, t)$ therefore gives the extent to which the surface deviates from the flat steady-state solution $h(x, y, t) = -v_0 t$. Equation (1) becomes

$$u_t = -A(\nabla u)^2 + C(\nabla u)^4 + C' u_x^2 u_y^2, \quad (4)$$

where $A \equiv \Omega J a$ and $C \equiv \Omega J c$ are positive and $C' \equiv \Omega J c'$.

If we only take sputtering into account, then the surface will in general develop points where the slope changes discontinuously as a function of position and then it will become multiple valued, i.e., overhangs will form. To eliminate this unphysical possibility for the case in which material **B** remains crystalline, we include the effect of thermally activated surface diffusion in the EOM (4). We will adopt the form of the surface diffusion term that is valid for small slopes for the sake of simplicity. Equation (4) then becomes

$$u_t = -A(\nabla u)^2 + C(\nabla u)^4 + C'u_x^2 u_y^2 - B\nabla^2 \nabla^2 u - B'u_{xyy}, \quad (5)$$

where B and B' are constants and $B > 0$. If material **B** is amorphous, then Eq. (5) still applies but the term $-B\nabla^2 \nabla^2 u$ comes from viscous flow near the surface of the solid rather than from surface diffusion [22]. Because there is complete rotational invariance in this case, $B' = 0$. In contrast, if material **B** is a crystalline material with fourfold rotational symmetry, then B' could be nonzero.

In keeping with our stated goal of constructing a minimal model that produces sputter cones, Eq. (5) omits a number of physical effects that could influence the dynamics but, as we shall see, these are not essential to the formation of sputter cones. Equation (5) does not include the effects of curvature-dependent sputtering [23,24] and ion-induced mass redistribution [25–27], for example. The effects of nonlocal phenomena like redeposition of sputtered material and sputtering by reflected ions have also been omitted.

Our choice of sputter yield (3) is not meant to accurately describe the yield for any particular choice of target material and ion beam. Instead, we have adopted it in the interest of constructing a model that is as simple and tractable as possible. Our $Y(u_x, u_y)$ has a maximum as $|\nabla u|$ is increased in the rotationally invariant case, as required. We will also see that the conclusions we will arrive at are to some extent robust: We will show that another form of the sputter yield leads to comparable results, although, in that case, we were unable to obtain any results analytically and so only carried out simulations.

We can reduce the number of parameters in the EOM by rescaling. We introduce the dimensionless variables

$$\begin{aligned} \tilde{x} &\equiv \left(\frac{A^3}{B^2 C}\right)^{1/6} x, & \tilde{y} &\equiv \left(\frac{A^3}{B^2 C}\right)^{1/6} y, & \tilde{t} &\equiv \left(\frac{A^6}{BC^2}\right)^{1/3} t, \\ \text{and} & & \tilde{u} &\equiv \left(\frac{C}{B}\right)^{1/3} u, \end{aligned} \quad (6)$$

and drop the tildes. Equation (5) becomes

$$u_t = -(\nabla u)^2 + (\nabla u)^4 + \gamma u_x^2 u_y^2 - \nabla^2 \nabla^2 u - 4\beta u_{xyy}, \quad (7)$$

where $\beta \equiv B'/(4B)$ and $\gamma \equiv C'/C$ are dimensionless. There are two dimensionless parameters in Eq. (7). In the isotropic case, $\beta = \gamma = 0$ and the EOM (7) is parameter free; this is yet another virtue of the choice of Y given by Eq. (3).

Consider a surface disturbance u that depends only on the time t and $\xi \equiv \hat{e} \cdot \mathbf{x}$, where $\mathbf{x} \equiv x\hat{x} + y\hat{y}$ and the unit vector $\hat{e} \equiv \hat{x} \cos \phi + \hat{y} \sin \phi$ lies in the x - y plane and makes the angle

ϕ with the x axis. For such a disturbance, Eq. (7) reduces to

$$\begin{aligned} u_t &= -u_\xi^2 + (1 + \gamma \cos^2 \phi \sin^2 \phi) u_\xi^4 \\ &\quad - (1 + 4\beta \cos^2 \phi \sin^2 \phi) u_{\xi\xi\xi\xi}. \end{aligned} \quad (8)$$

We require that the sputter yield have a maximum as u_ξ is increased for all values of ϕ . This leads to the requirement that $\gamma > -4$. Similarly, we insist that the final term on the right-hand side of Eq. (8) have a negative coefficient so that short wavelength disturbances are smoothed away. This leads to the requirement that $\beta > -1$. Both of these conditions are satisfied in the isotropic case in which $\beta = \gamma = 0$.

III. ANALYSIS OF THE EQUATION OF MOTION

A. One dimension

For the 1D case in which u depends only on x and t , Eq. (7) reduces to

$$u_t = -u_x^2 + u_x^4 - u_{xxxx}, \quad (9)$$

which is parameter free. Setting $b \equiv u_x$ and differentiating Eq. (9) with respect to x , we obtain

$$b_t + \partial_x Y(b) = -b_{xxxx}, \quad (10)$$

where

$$Y(b) \equiv b^2 - b^4 \quad (11)$$

is the rescaled sputter yield.

Equation (10) has been studied in detail by Chen *et al.* [28] and by Holmes-Cerfon *et al.* [29,30] for general choices of the function $Y(b)$. For the sake of completeness, we will summarize the results of their analysis before specializing to the yield given by Eq. (11). (To be perfectly precise, the term on the right-hand side of the equation analogous to Eq. (10) found in Refs. [28–30] has a more complex form that reduces to ours for small slopes b . This, however, does not affect the analysis.)

If the right-hand side of Eq. (10) were zero, then we would have

$$b_t + \partial_x Y(b) = 0. \quad (12)$$

This can be thought of as the continuity equation for the conserved quantity b ; the “flux” of b is $Y(b)$. Equation (12) can also be written $b_t + Y'(b)b_x = 0$, which shows that $Y'(b)$ is the advection velocity. A small disturbance to a surface of slope b_0 propagates with velocity $Y'(b_0)$.

Shock waves can form if $Y'(b)$ depends on b (and it does in our problem). If Eq. (12) were the EOM, then a shock could steepen without limit and, past a certain time, the height of the surface would no longer be single valued. The presence of the smoothing term $-b_{xxxx}$ in Eq. (10) prevents b_x from growing without bound and the surface height remains single valued.

To find shock-wave solutions to Eq. (10), one seeks traveling-wave solutions of the form $b = b(\xi)$, where $\xi \equiv x - ct$ and c is the propagation velocity of the shock [29,30]. We require that $b(\xi) \rightarrow b_l$ for $\xi \rightarrow -\infty$ and $b(\xi) \rightarrow b_r$ for $\xi \rightarrow \infty$, where the asymptotic values b_l and b_r are constants. c is given by the Rankine-Hugoniot condition [31]

$$c = \frac{Y(b_l) - Y(b_r)}{b_l - b_r}, \quad (13)$$

and so the shock's velocity is determined if b_l and b_r are given.

Classical (compressive) shocks satisfy the Lax entropy condition

$$c_r < c < c_l, \quad (14)$$

where $c_l \equiv Y'(b_l)$ and $c_r \equiv Y'(b_r)$ are the advection velocities to the left and right of the shock, respectively. Surface disturbances on either side of the shock propagate toward the shock in this case, i.e., the shock is "compressed." By definition, (singly) undercompressive shocks violate one of the inequalities (14), while doubly undercompressive shocks violate both. In the case of classical shocks, the permissible pairs of values (b_l, b_r) form a two-dimensional region (or regions) in the parameter space with coordinates b_l and b_r . In contrast, for singly undercompressive shocks, once b_l has been specified, the value of b_r is either determined or does not exist. These solutions make a curve in the parameter space. Finally, doubly undercompressive shocks exist only for certain choices of b_l and b_r if they exist at all. The permissible pairs of values (b_l, b_r) are isolated points in the parameter space.

In our problem, $Y(b)$ is given by Eq. (11). We wish to find a shock-wave solution that is a one-dimensional analog of a sputter cone, and so we want $b_l > 0$ and $b_r = -b_l$. Equation (13) shows that the propagation velocity c of such a shock is zero, since $Y(b)$ is an even function of b . In fact, because the height of the cone should be an even function of x , it follows that $c = 0$ by symmetry.

We seek solutions to Eq. (9) of the form $u(x, t) = f(x) - v_0 t$, where $f(x)$ gives the shape of the cone and v_0 is the rate it moves downward as a result of erosion. Setting $g \equiv f_x$, we find that g must satisfy

$$-g^2 + g^4 - g_{xxx} = -v_0, \quad (15)$$

where $g(0) = 0$. We seek solutions to Eq. (15) of the form

$$g(x) = \mathcal{A} \tanh(\kappa x), \quad (16)$$

where \mathcal{A} and κ are constants. Inserting our solution ansatz (16) into Eq. (15) and equating the coefficients of like powers of $\tanh(\kappa x)$, we get three algebraic equations that relate \mathcal{A} , κ and v_0 . These equations have only one solution, which is given by $\mathcal{A} = -\sqrt{3}/2$, $\kappa = 3^{1/6}/2^{4/3}$ and $v_0 = 3/16$. Thus, we have

$$b(x, t) = g(x) = -\frac{\sqrt{3}}{2} \tanh\left(\frac{3^{1/6}}{2^{4/3}}x\right). \quad (17)$$

Note that $g(0) = 0$, as required, and that $b \rightarrow \mp\sqrt{3}/2$ for $x \rightarrow \pm\infty$. There is a sputter cone solution only for the asymptotic values of the slope $b_l = \sqrt{3}/2$ and $b_r = -\sqrt{3}/2$; we will refer to these as the selected slopes.

We find f by integrating Eq. (17) with respect to x . This leads to our final result,

$$u(x, t) = -6^{1/3} \ln \left[\cosh\left(\frac{3^{1/6}}{2^{4/3}}x\right) \right] - \frac{3}{16}t + K, \quad (18)$$

where K is a constant of integration. As we shall see in Sec. V, for a wide variety of initial conditions, the surface height tends toward the solution given by Eq. (18).

For the shock solution given by Eqs. (17) and (18), $c = 0$, $b_l = \sqrt{3}/2$ and $b_r = -\sqrt{3}/2$. Therefore

$c_l = Y'(b_l) = -\sqrt{3}/2$ and $c_r = Y'(b_r) = \sqrt{3}/2$. It follows that

$$c_l < c < c_r, \quad (19)$$

i.e., both of the inequalities in the Lax entropy condition (14) are violated. The shock we have found is therefore doubly undercompressive. This means that a small disturbance on the side of the cone will propagate away from the cone's tip.

It is important to note that the sputter cone solution we have found has sides with fixed slope $\sqrt{3}/2$. The apex angle of the cone therefore has only one possible value. This is a consequence of the fact that the shock is doubly undercompressive.

Far from the cone's apex, its sides have a dimensionless slope of magnitude $\sqrt{3}/2$. In the original units, this slope is $(3A/4C)^{1/2}$. The radius of curvature of the cone's apex is $4(2BC^2/9A^3)^{1/3}$ in the original units. This decreases if B is reduced. In the limit that B tends to zero, the slope changes discontinuously at the tip of the cone. A slope discontinuity in the limit that the coefficient of the smoothing term tends to zero is a key property of a shock wave [31].

B. Two dimensions

In the 2D case, u depends on x , y , and t . There is a particularly interesting special case in which $\gamma = -2$ and Eq. (7) becomes

$$u_t = -u_x^2 + u_x^4 - u_{xxx} - u_y^2 + u_y^4 - u_{yyy} - (2 + 4\beta)u_{xyy}. \quad (20)$$

Suppose that $u_1(x, t)$ and $u_2(x, t)$ are both solutions to the 1D EOM (9). It is easy to see that

$$u(x, y, t) = u_1(x, t) + u_2(y, t) \quad (21)$$

is then a solution to the 2D EOM (20), no matter what the value of β is. Thus, for the case $\gamma = -2$, we can find solutions to the 2D problem by solving the 1D problem. In particular, we have the solution constructed by taking u_1 and u_2 to be doubly undercompressive shocks:

$$u(x, y, t) = -6^{1/3} \{ \ln[\cosh(\kappa x)] + \ln[\cosh(\kappa y)] \} - \frac{3}{8}t + 2K, \quad (22)$$

where K is an arbitrary constant and we remind the reader that $\kappa = 3^{1/6}/2^{4/3}$. Equation (22) describes a four-sided pyramid with a rounded tip and edges, as shown in Fig. 1. The pyramid is fourfold rotationally symmetric. If it were not for the rounding of the pyramid's tip and edges, then its four faces would all have slope $\sqrt{3}/2$. In addition, if the pyramid's edges were projected onto the x - y plane, then they would coincide with the lines $x = 0$ and $y = 0$.

Equation (7) can also be decoupled into two 1D problems for $\gamma = 4$. In this case, we introduce coordinate axes ξ and η that are obtained by rotating the x and y axes by 45° , i.e., we introduce the new coordinates $\xi \equiv (x + y)/\sqrt{2}$ and

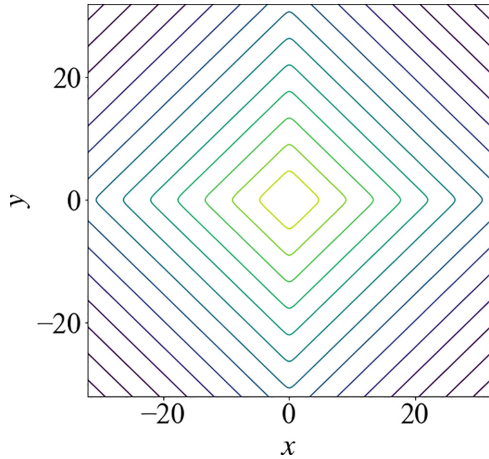


FIG. 1. A contour plot of the 2D analytical solution (22) for the surface height u . The highest (lowest) contours are shown in light green (violet).

$\eta \equiv (-x + y)/\sqrt{2}$. Equation (7) becomes

$$u_t = -u_\xi^2 + 2u_\xi^4 - (1 + \beta)u_{\xi\xi\xi\xi} - u_\eta^2 + 2u_\eta^4 - (1 + \beta)u_{\eta\eta\eta\eta} - 2(1 - \beta)u_{\xi\xi\eta\eta}. \quad (23)$$

We now set $\tilde{\xi} \equiv 2^{-1/6}(1 + \beta)^{-1/3}\xi$, $\tilde{\eta} \equiv 2^{-1/6}(1 + \beta)^{-1/3}\eta$, $\tilde{t} = 2^{-2/3}(1 + \beta)^{-1/3}t$, and $\tilde{u} \equiv 2^{1/3}(1 + \beta)^{-1/3}u$. Equation (23) is then

$$\tilde{u}_{\tilde{t}} = -\tilde{u}_{\tilde{\xi}}^2 + \tilde{u}_{\tilde{\xi}}^4 - \tilde{u}_{\tilde{\xi}\tilde{\xi}\tilde{\xi}\tilde{\xi}} - \tilde{u}_{\tilde{\eta}}^2 + \tilde{u}_{\tilde{\eta}}^4 - \tilde{u}_{\tilde{\eta}\tilde{\eta}\tilde{\eta}\tilde{\eta}} - 2(1 - \beta)(1 + \beta)^{-1}\tilde{u}_{\tilde{\xi}\tilde{\xi}\tilde{\eta}\tilde{\eta}}. \quad (24)$$

Note the close analogy between Eqs. (20) and (24); we see that Eq. (24) has solutions of the form $\tilde{u} = u_1(\tilde{\xi}, \tilde{t}) + u_2(\tilde{\eta}, \tilde{t})$, where u_1 and u_2 are solutions to the 1D EOM. In particular, we have the solution

$$\tilde{u}(\tilde{\xi}, \tilde{\eta}, \tilde{t}) = -6^{1/3}\{\ln[\cosh(\kappa\tilde{\xi})] + \ln[\cosh(\kappa\tilde{\eta})]\} - \frac{3}{8}\tilde{t} + 2\tilde{K}, \quad (25)$$

where \tilde{K} is an arbitrary constant. This solution is a four-sided pyramid with a rounded tip and edges, but it is rotated by 45° about the z axis relative to the pyramid we found for the case $\gamma = -2$. When written in terms of the original variables, Eq. (25) is

$$u(x, y, t) = -3^{1/3}(1 + \beta)^{1/3} \times \left(\ln \left\{ \cosh \left[\frac{3^{1/6}}{4(1 + \beta)^{1/3}}(x + y) \right] \right\} + \ln \left\{ \cosh \left[\frac{3^{1/6}}{4(1 + \beta)^{1/3}}(-x + y) \right] \right\} \right) - \frac{3}{16}t, \quad (26)$$

where we have set $\tilde{K} = 0$. We can rewrite Eq. (26) in a form that does not depend on the parameter β by setting $\bar{x} = (1 + \beta)^{-1/3}x$, $\bar{y} = (1 + \beta)^{-1/3}y$ and $\bar{u} = (1 + \beta)^{-1/3}u$. This

yields

$$\bar{u}(\bar{x}, \bar{y}, t) = -3^{1/3} \left(\ln \left\{ \cosh \left[\frac{3^{1/6}}{4}(\bar{x} + \bar{y}) \right] \right\} + \ln \left\{ \cosh \left[\frac{3^{1/6}}{4}(-\bar{x} + \bar{y}) \right] \right\} \right) - \frac{3}{16}t. \quad (27)$$

Equations (20) and (24) show that the problems with $\gamma = -2$ and $\gamma = 4$ are in fact formally identical: One problem is obtained from the other by carrying out a 45° rotation and rescaling. It is therefore sufficient to consider one of these two problems. We will restrict our attention to the case $\gamma = 4$ because in that case the sputter cone fits neatly into the domain we used in our simulations, $\{(x, y) | -L \leq x \leq L \text{ and } -L \leq y \leq L\}$.

We will also be interested in the isotropic case in which $\beta = \gamma = 0$ and the EOM (7) reduces to

$$u_t = -(\nabla u)^2 + (\nabla u)^4 - \nabla^2 \nabla^2 u. \quad (28)$$

The 2D problem cannot be separated into two 1D problems in this case. Some simplification is possible, though, if the initial surface configuration is rotationally symmetric. In this case, u only depends on t and the radial distance $r \equiv \sqrt{x^2 + y^2}$ for $t \geq 0$. Equation (28) is then

$$u_t = -u_r^2 + u_r^4 - \left[\frac{1}{r} \frac{\partial}{\partial r} \left(r \frac{\partial}{\partial r} \right) \right]^2 u. \quad (29)$$

We seek solutions to Eq. (29) of the form $u(r, t) = -v_0 t + F(r)$ and set $G = F_r$. The function $G(r)$ must satisfy

$$-v_0 = -G^2 + G^4 - \left[\frac{1}{r} \frac{d}{dr} \left(r \frac{d}{dr} \right) \right] \left[\frac{1}{r} \frac{d}{dr} (rG) \right]. \quad (30)$$

A sputter cone is a solution to this third-order ordinary differential equation with $G = u_r = 0$ for $r = 0$ and with $G = u_r \rightarrow -s$ and $G_r = u_{rr} \rightarrow 0$ for $r \rightarrow \infty$, where the positive constant s is the slope of the cone far from its apex. Taking the $r \rightarrow \infty$ limit of Eq. (30) gives

$$-v_0 = -s^2 + s^4. \quad (31)$$

Equation (30) is analogous to the equation we obtained in 1D, Eq. (15). In contrast to the situation in 1D, however, we have been unable to find an analytical solution to Eq. (30). Our study of the isotropic case in 2D will therefore be entirely numerical.

IV. A GENERALIZATION OF THE MODEL

To this point, we have not included terms in the EOM that are proportional to second-order spatial derivatives of the surface height. In the case of an amorphous or amorphized target material, terms of this kind can come from curvature-dependent sputtering [24] and mass redistribution [25–27]. In the case of a target material that remains crystalline during the ion irradiation, on the other hand, the Ehrlich-Schwoebel (ES) effect can produce such a term [32–35].

For the sake of simplicity, in this section we will restrict ourselves to the 1D case in which the surface height u is independent of y . Including a second-order term, the 1D EOM

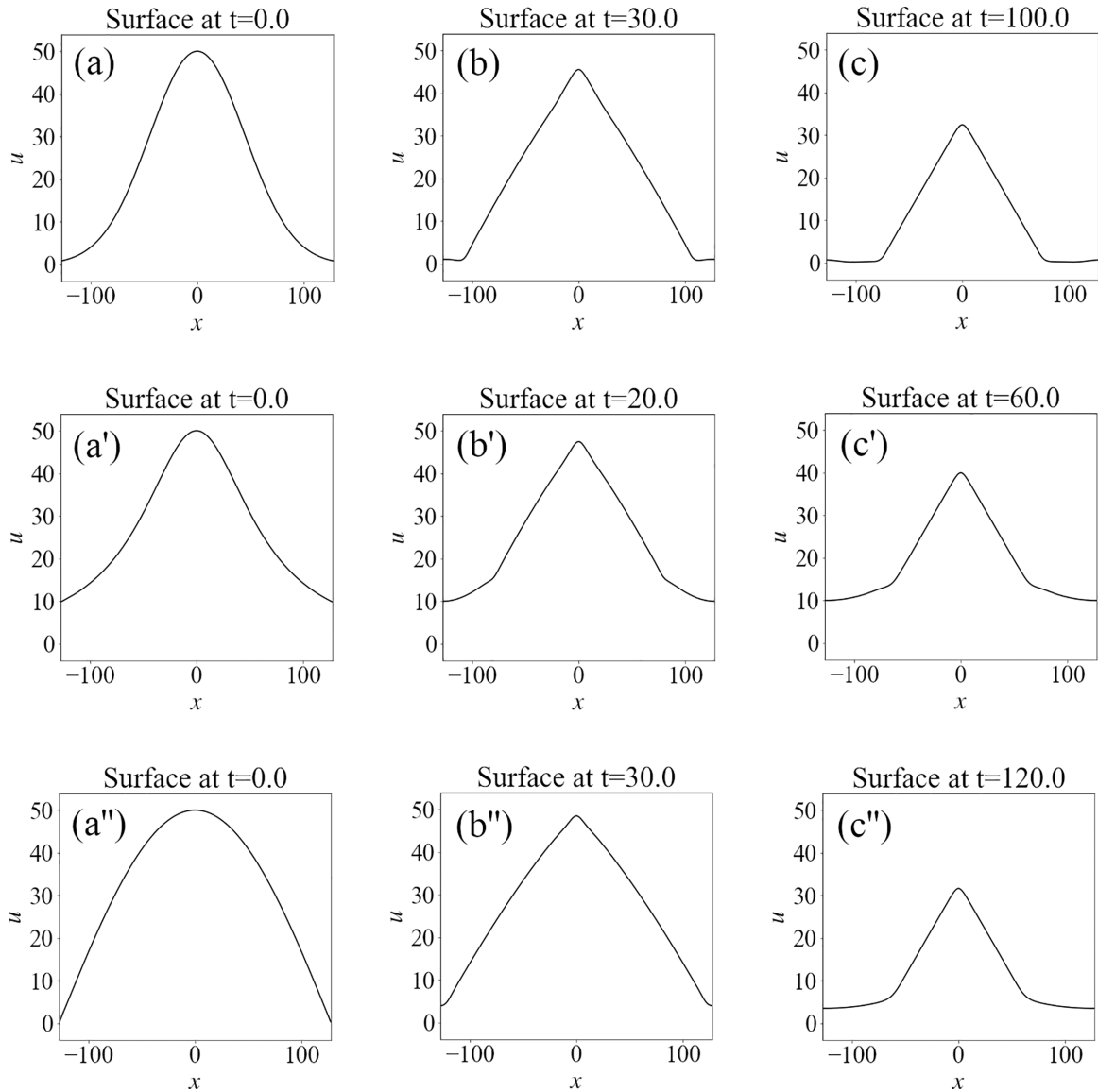


FIG. 2. Simulations of the 1D EOM (9) for three initial conditions: (a) a Gaussian, (a') a Lorentzian, and (a'') a half wavelength of a sine wave. The graphs (b)–(b'') show the respective surfaces at later times when the cones are beginning to emerge, while the graphs (c)–(c'') show the surfaces at still later times when the cones are nearly fully formed. The respective times are shown above each panel.

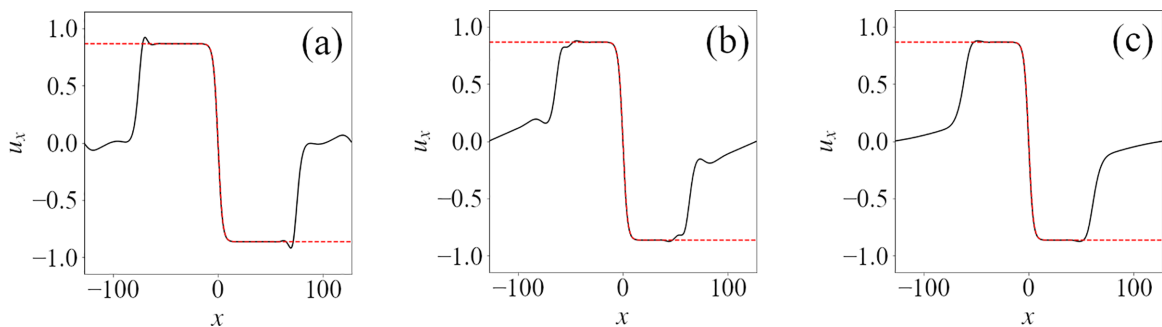


FIG. 3. Plots of the slopes of the cones shown in Figs. 2(c)–2(c''), corresponding to (a) the Gaussian initial condition, (b) the Lorentzian initial condition, and (c) the half-wavelength sine initial condition. The red dashed curves are plots of the analytical solution for u_x given by Eq. (17).

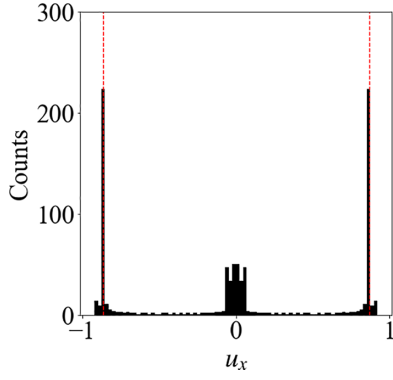


FIG. 4. The slope distribution for the surface shown in Fig. 2(c). The red dashed lines are located at $u_x = \pm\sqrt{3}/2$.

(5) becomes

$$u_t = -Au_x^2 + Cu_x^4 - Bu_{xxxx} + \delta u_{xx}, \quad (32)$$

where δ is a constant. After rescaling as before, Eq. (32) is recast as

$$u_t = -u_x^2 + u_x^4 - u_{xxxx} + Du_{xx}, \quad (33)$$

where $D \equiv (C/B)^{1/3}\delta/A$ is dimensionless. The new term that has been appended to the right-hand side of Eq. (9) has a stabilizing (destabilizing) effect for positive (negative) values of the parameter D . If D is negative, then a flat surface with zero slope is linearly unstable. Typically, if the target material is amorphized by the ion bombardment, then the stabilizing effect of mass redistribution is stronger than the destabilizing effect of curvature-dependent sputtering for normal incidence bombardment and so D is positive. In any event, because we wish to study sputter cone formation that is seeded by the presence of a second atomic species rather than the spontaneous formation of cones, we will restrict our attention to the case $D \geq 0$. The constant D is then a dimensionless measure of the net strength of the second-order smoothing term.

For $D > 0$, we again seek solutions to the EOM of the form $u(x, t) = f(x) - v_0 t$. Equation (33) shows that the function $g \equiv f_x$ must satisfy

$$-g^2 + g^4 - g_{xxx} + Dg_x = -v_0. \quad (34)$$

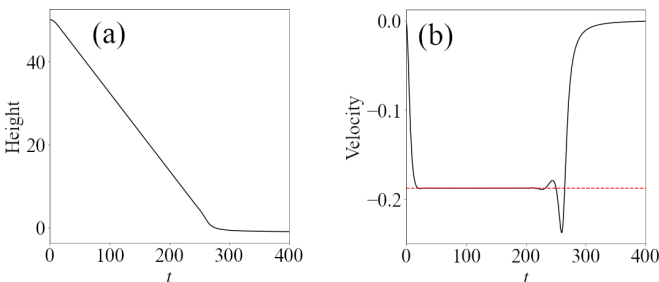


FIG. 5. The (a) height $u(0, t)$ and (b) recession velocity $u_t(0, t)$ of the cone's tip at $x = 0$ versus time, beginning with the initial condition shown in Fig. 2(a). The red dashed line on the velocity graph is located at the predicted tip velocity, $-v_0 = -3/16$.

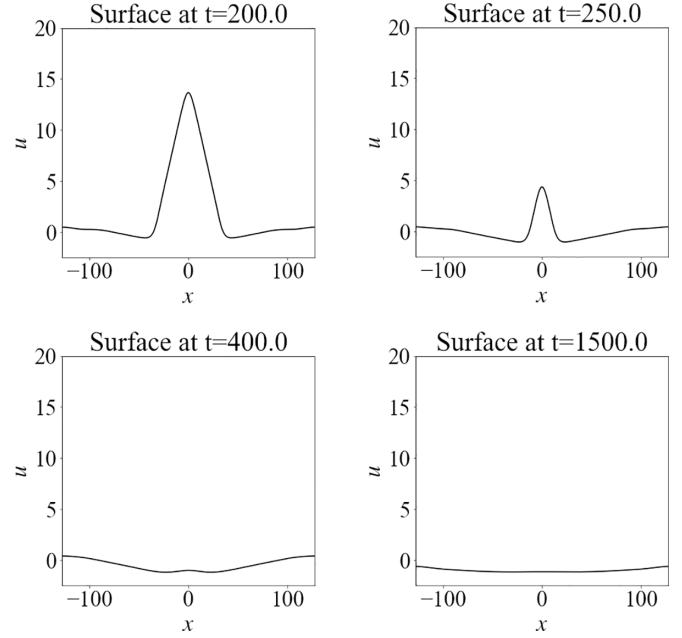


FIG. 6. The simulation with the Gaussian initial condition shown in Fig. 2(a) at later times.

We seek solutions to Eq. (34) of the form given by Eq. (16). We find that

$$\mathcal{A} = -\frac{\sqrt{3}}{2} \left(1 - \frac{D}{D_c}\right)^{1/2}, \quad (35)$$

$$\kappa = \frac{3^{1/6}}{2^{4/3}} \left(1 - \frac{D}{D_c}\right)^{1/2}, \quad (36)$$

and

$$v_0 = \frac{3}{16} \left(1 - \frac{D}{D_c}\right) \left(1 + 3\frac{D}{D_c}\right), \quad (37)$$

where $D_c \equiv 6^{1/3}$. The surface height is given by

$$u(x, t) = \frac{\mathcal{A}}{\kappa} \ln[\cosh(\kappa x)] - v_0 t + u_0, \quad (38)$$

where u_0 is an arbitrary constant. Thus, we have a sputter cone solution for values of D less than the critical value D_c ; no such solution exists for $D > D_c$ because \mathcal{A} and κ are imaginary in this case. For $0 \leq D \leq D_c$, the slope of the flanks of the cone $|\mathcal{A}|$ decreases as D is increased. From a physical standpoint, this is because the strength of the second-order smoothing term increases with D . Naturally, the solution given by Eqs. (35)–(38) reduces to the one we obtained earlier [Eq. (18)] if we set D to zero.

There is no sputter cone solution for $B \rightarrow 0$ since $D \equiv (C/B)^{1/3}\delta/A$ exceeds $D_c = 6^{1/3}$ in that limit. This shows that the fourth-order smoothing term is essential to the formation of an undercompressive shock. In fact, this was already noted in work on the undercompressive shocks that develop when a fluid thin film flows down an inclined plane in the presence of a thermal gradient [36,37]. The importance of a nonconvex flux was also emphasized in that context, and, indeed, the flux $Y(b) = b^2 - b^4$ is not a convex function of b in our model of sputter cone formation.

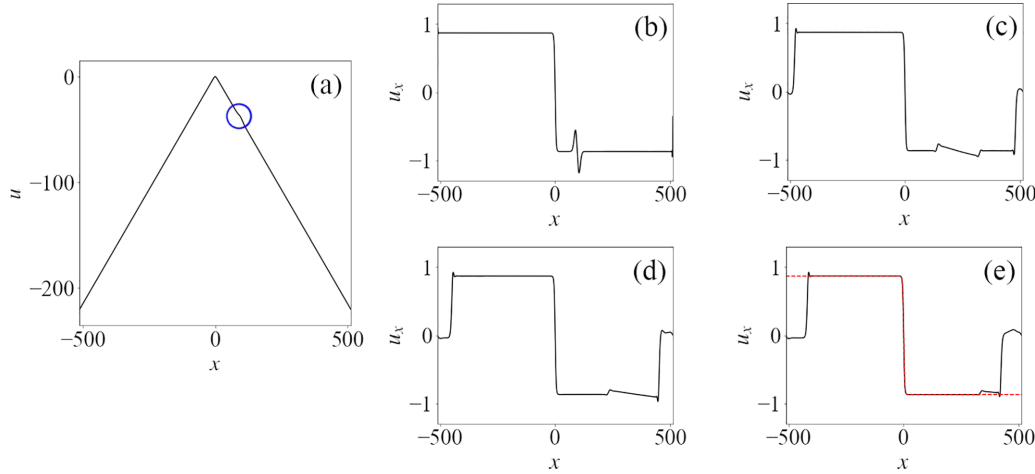


FIG. 7. A simulation of the 1D EOM (9) with $L = 512$. The initial condition, which is shown in (a), was the sputter cone solution (18) with a Gaussian perturbation placed on its side. The perturbation is at the center of the blue circle. The slope of the surface is shown at (b) $t = 0$, (c) $t = 75$, (d) $t = 150$, and (e) $t = 225$. The analytical solution for the cone’s slope is shown with the red dashed line in (e). As time passes, the perturbation moves down the side of the cone, away from its tip. The perturbation also broadens as its amplitude decreases.

To further illustrate these ideas, consider the behavior if both the fourth-order smoothing term $-u_{xxxx}$ and the quartic nonlinearity u_x^4 are omitted from Eq. (33) and D is positive. The resulting equation is

$$u_t + u_x^2 = Du_{xx}. \quad (39)$$

Differentiating Eq. (39) with respect to x , setting $\tilde{b} = 2b = 2u_x$, and then dropping the tildes, we obtain Burgers’s equation [31]

$$b_t + bb_x = Db_{xx}. \quad (40)$$

In this approximation, the flux is $b^2/2$, which is convex, and of course the fourth-order smoothing term is absent.

Equation (40) has the shock-wave solution

$$b(x, t) = \frac{1}{2}(b_l + b_r) - \frac{1}{2}(b_l - b_r) \tanh \left[\frac{b_l - b_r}{4D}(x - ct) \right], \quad (41)$$

where $b \rightarrow b_r$ for $x \rightarrow \infty$, $b \rightarrow b_l$ for $x \rightarrow -\infty$, and $c \equiv (b_l + b_r)/2$ the velocity of the shock [31]. Equation (41) is a classical (compressive) shock. It is a valid solution to Eq. (40) for any $b_l > b_r$. Thus, there are no selected slopes in this simple approximation. Both the fourth-order smoothing term and the term u_x^4 that appear in Eq. (33) are needed if sputter cones with selected slopes are to form.

For a sputter cone with selected slopes to develop from a surface protrusion that is present initially, the protrusion must be sufficiently high and narrow. To see this, suppose that $D > 0$ and $u(x, 0) = U(X, 0)$, where $X \equiv \epsilon x$ and ϵ is small. $u(x, 0)$ is then a slowly varying function of x , and the surface slope $u_x(x, 0) = \epsilon U_X(X, 0)$ is small. We seek solutions to our generalized EOM (33) of the form $u(x, t) = U(X, T)$, where $T \equiv \epsilon^2 t$. In the language of the method of multiple scales, x and t are the “fast” position and time, whereas X and T are the corresponding “slow” variables. Equation (33) becomes

$$\epsilon^2 U_T = \epsilon^2 (-U_X^2 + DU_{XX}) + \epsilon^4 (U_X^4 - U_{XXXX}). \quad (42)$$

Retaining only terms up to second order in ϵ , we obtain

$$U_T + U_X^2 = DU_{XX}. \quad (43)$$

As we saw in the preceding paragraph, Eq. (43) has no sputter cone solutions with selected slopes. We conclude that for a sputter cone with selected slopes to develop, the initial surface protrusion must be sufficiently high and narrow, as claimed.

V. SIMULATIONS

A. Simulations in 1D

The 1D EOM (9), as well as the generalized 1D EOM (33), were integrated numerically using the

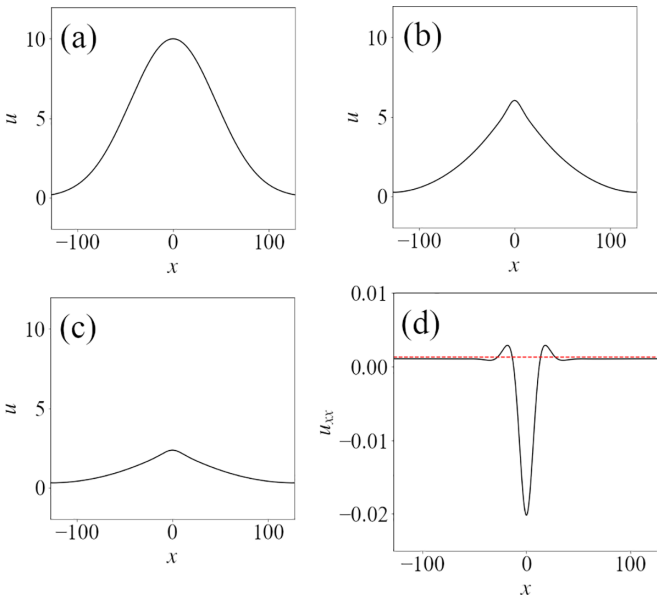


FIG. 8. A simulation with a Gaussian initial condition with $u_0 = 10$ and $\sigma^2 = 500$. The surface is shown at (a) $t = 0$, (b) $t = 100$, and (c) $t = 400$. A plot of u_{xx} for the surface in (c) is shown in (d). The red dashed line is located at $u_{xx} = 1/2t$.

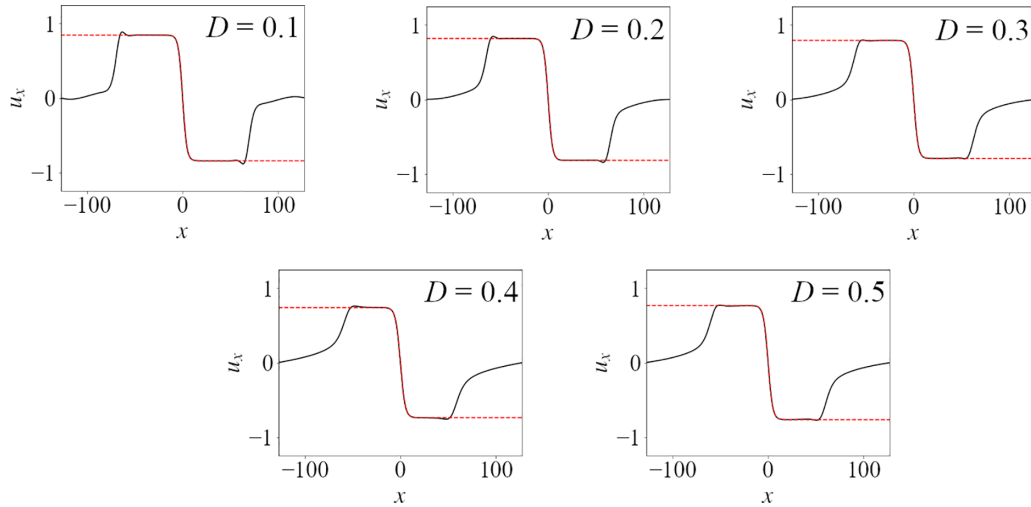


FIG. 9. Plots of u_x for sputter cones formed from the Gaussian initial condition in Fig. 2(a) at time $t = 100$ for various values of D . The red dashed plots of u_x were obtained from Eq. (38) with parameter values given by Eqs. (35)–(37).

fourth-order Runge-Kutta exponential time-differencing (ETD4RK) method described by Cox and Matthews [38] on the domain $-L \leq x \leq L$. We set $L = 128$ and used $N = 1024$ grid points unless otherwise stated. Periodic boundary conditions were applied. The linear terms were calculated in Fourier space while the nonlinear terms were computed in real space using a central differencing scheme accurate to fourth order in the grid spacing. Simulations were carried out for initial conditions with surface protrusions of various kinds.

Figure 2 shows the results of simulations carried out with $D = 0$ for three different initial conditions that have surface protrusions. The protrusions evolved into sputter cones in all three cases. While the evolution of the surfaces and the times required for the sputter cones to form differed, the resulting cones are nearly identical. Figure 3 shows plots of the surface slope for the surfaces shown in Figs. 2(c)–2(c’). There are regions of appreciable width in which the slope is close to one of the two predicted values, $u_x = \pm\sqrt{3}/2$; these regions are the sides of the cones. Also shown in Figs. 3(a)–3(c) is the analytical solution for u_x given by Eq. (17). For all three initial conditions, the slope of the cone is in very good agreement with the predicted form both on the sides of the cone and in the vicinity of its tip. Figure 4 gives the distribution of slopes for the cone formed from the Gaussian initial condition. The two peaks in the wings of the distribution come from the

sides of the cone and are centered on the predicted slopes, $u_x = \pm\sqrt{3}/2$. The large number of occurrences of slopes near zero, on the other hand, is due to the two regions that flank the cone in which the slope is relatively small. Note, too, that the slope distribution is symmetric about $u_x = 0$, as it should be. Figure 5 shows that, after a brief transient, the cone recedes into the surface at the predicted constant velocity $-v_0 = -3/16$ for the initial condition in Fig. 2(a), showing further agreement with Eq. (18). The time interval in which a cone persists is dependent on the form of the initial protrusion, but after some time has passed, any cone will completely recede into the ambient surface because the erosion rate is higher on the sides of the cone than on the relatively flat regions beside it. This kind of time evolution—which is illustrated by Fig. 6—is analogous to what is seen in experiments: All sputter cones have a finite lifetime.

As noted earlier, a sputter cone is a doubly undercompressive shock, and a small disturbance on the side of a cone will propagate away from the cone’s apex. This is illustrated by the simulation shown in Fig. 7.

The Gaussian initial condition shown in Fig. 2(a) is given by

$$u(x, 0) = u_0 e^{-x^2/2\sigma^2}, \tag{44}$$

where $u_0 = 50$ and $\sigma^2 = 500$. If the value of u_0 is reduced below a threshold value, then the time evolution of the

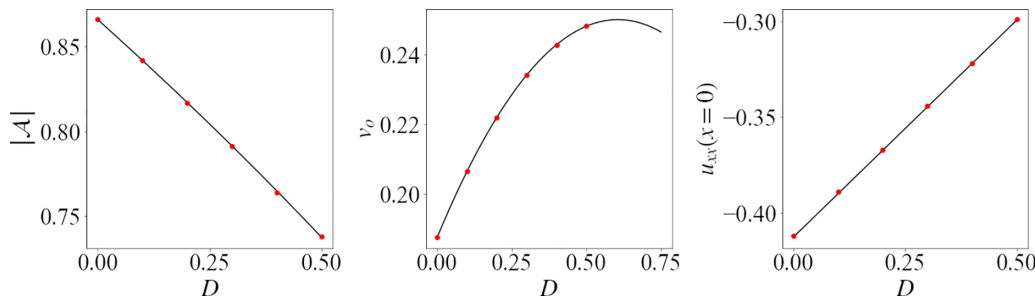


FIG. 10. Plots of $|A|$, v_0 , and the value of u_{xx} at $x = 0$ versus D . The black curves show the predictions of Eqs. (35)–(38), while the red dots show the values obtained from the simulations for the five selected positive values of D .

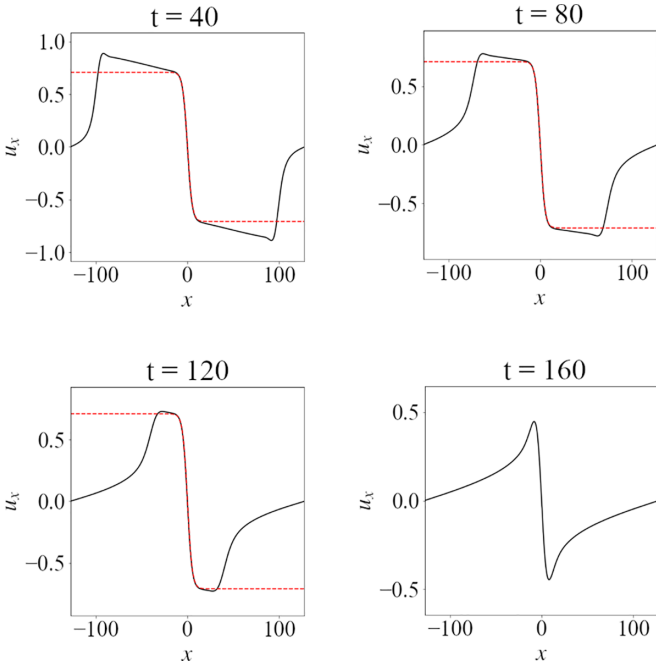


FIG. 11. A simulation with $D = 0.6$ starting with the Gaussian initial condition shown in Fig. 2(a). While the surface seems to be tending towards the analytical steady-state solution shown with the red dashed curves, the protrusion recedes into the ambient surface before the cone has fully formed.

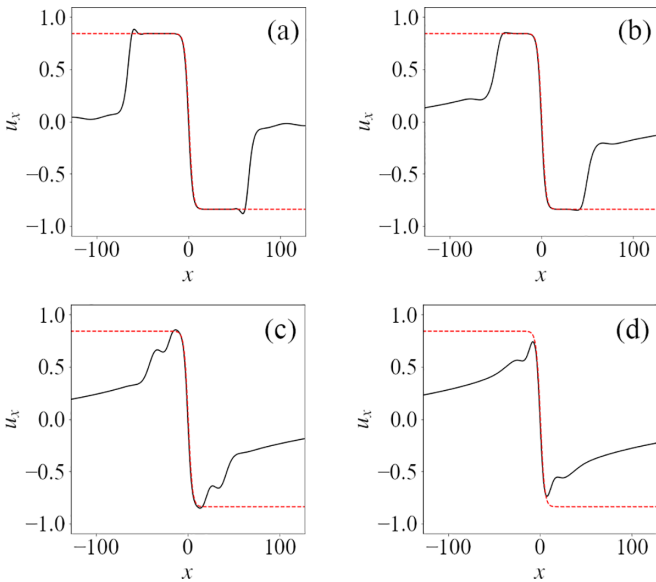


FIG. 12. Plots of u_x versus x for simulations of the generalized 1D EOM (33) with $D = 0.1$ and $L = 512$ at $t = 110$ for the Gaussian initial condition (44) with $u_0 = 50$ and four values of σ^2 . The σ^2 values are as follows: (a) $\sigma^2 = 500$, (b) $\sigma^2 = 1250$, (c) $\sigma^2 = 2000$, and (d) $\sigma^2 = 2750$. The red dashed curves show the analytical steady-state solution for u_x . Note that while the simulations were carried out on the domain with $-512 \leq x \leq 512$, only the region with $-128 \leq x \leq 128$ is shown in the plots.

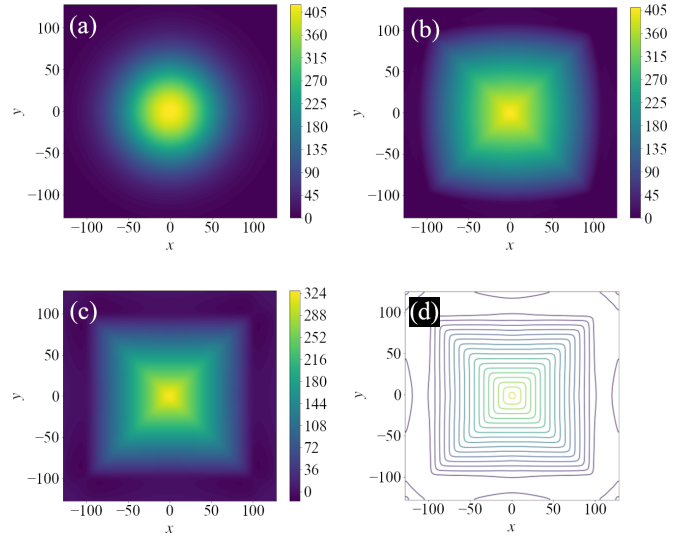


FIG. 13. A simulation of Eq. (7) with $\beta = 0$ and $\gamma = 4$. Panel (a) shows the initial Gaussian protrusion, panel (b) shows the surface at time $t = 100$, and panel (c) shows the surface at time $t = 550$. The false color rulers indicate the surface height u . (d) A contour plot of the surface shown in (c).

protrusion is quite different and a sputter cone does not emerge. This is illustrated by Fig. 8, in which σ^2 is once again equal to 500 but the value of u_0 has been reduced to 10. In this case, regions in which the surface slope is nearly constant do not form; instead, the flanks of the protrusion become approximately parabolic. This is seen most clearly in Fig. 8(d), which shows u_{xx} as a function of x at time $t = 400$. Away from the tip of the protrusion, u_{xx} is nearly independent of x .

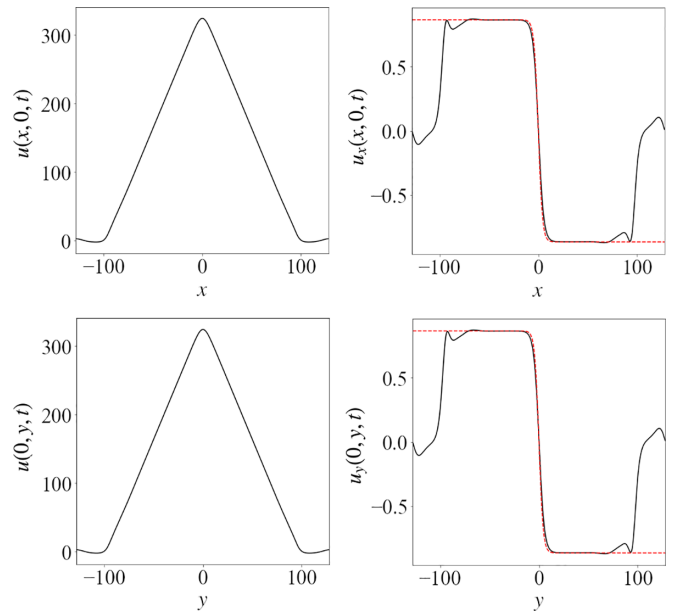


FIG. 14. Cross sections of the surface shown in Fig. 13(b) along the x and y axes together with their respective slopes, u_x and u_y . The red dashed plots show the the analytical solution for the slopes.

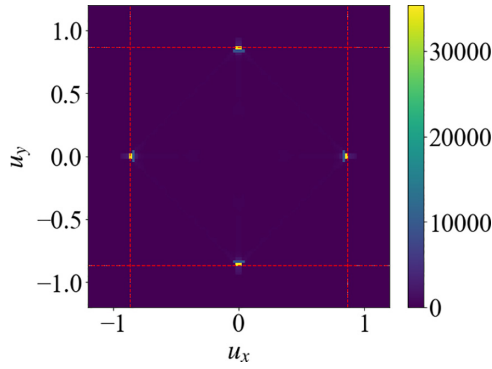


FIG. 15. The gradient distribution for the surface shown in Fig. 13(c). The false color ruler shows the number of counts for a given gradient. The red dashed lines are located at $u_x = \pm\sqrt{3}/2$ and $u_y = \pm\sqrt{3}/2$. Slope values near zero were excluded, which removes a bright peak centered on $(u_x, u_y) = (0, 0)$ that comes from the flatter regions flanking the sputter cone.

For small slopes, Eq. (9) can be approximated by

$$u_t = -u_x^2 - u_{xxxx}, \quad (45)$$

which has the solution

$$u(x, t) = \frac{(x - x_0)^2}{4t} + C, \quad (46)$$

where C and x_0 are constants. For this solution, $u_{xx} = (2t)^{-1}$. As seen in Fig. 8(d), on the sides of the protrusion, u_{xx} is very close to this value for large-enough times t .

If $u(x, t)$ is given by Eq. (46), then $u_x = (x - x_0)/2t$. The point where the slope u_x has the value s moves away from the point $x = x_0$ with constant speed $2s$ for all values of s . For this reason, the solution given by Eq. (46) is known as an expansion wave or rarefaction. Thus, when u_0 is sufficiently small, a sputter cone with sides of approximately constant slope does not develop; instead, the flanks of the protrusion evolve into rarefactions.

For positive values of D up to 0.5, we found good agreement between the steady-state analytical solution given by Eqs. (35)–(38) and simulations carried out with the Gaussian initial condition given by Eq. (44) with $u_0 = 50$ and $\sigma^2 = 500$. In Fig. 9, for example, u_x at time $t = 100$ is plotted

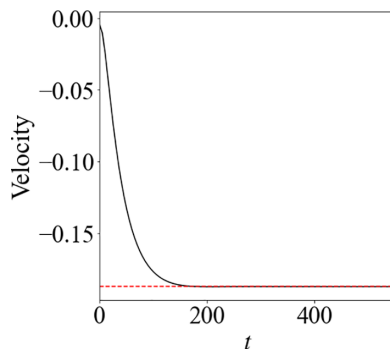


FIG. 16. The recession velocity $u_t(0, 0, t)$ of the sputter cone's tip at $x = y = 0$ versus time for the simulation shown in Fig. 13. The red dashed line is located at the predicted tip velocity, $-v_0 = -3/16$.

versus x for five different values of $D \leq 0.5$. Also shown in Fig. 9 is the surface slope obtained from Eqs. (35)–(38) for the five selected positive values of D ; the agreement with the simulations is excellent in all cases. The magnitude of the selected slope $|\mathcal{A}|$, the recession speed v_0 , and the value of u_{xx} at $x = 0$ as given by Eqs. (35)–(38) are plotted versus D in Fig. 10. Estimates of $|\mathcal{A}|$ and the value of u_{xx} at $x = 0$ were obtained from the simulated surfaces at time $t = 100$. To obtain an estimate of v_0 from the simulations, we found the average speed that the cone tip receded between the time when cone formed and when it receded into the ambient surface. These estimates are also shown in Fig. 10 for the five selected positive values of D . Once again, the agreement between the steady-state solution for the cone and the simulations is impressive.

As D is increased, the time that it takes for the surface to approach the predicted conical steady state increases. For D greater than 0.5, we do not observe the formation of extended regions in which the slope closely matches the predicted value before the incipient cone recedes into the ambient surface, as is seen for $D = 0.6$ in Fig. 11. However, if we choose the initial surface to be given by the analytical solution (38), then we find that the cone retains its shape until it is eventually sputtered away for D up to $D_c = 6^{1/3}$.

At the end of Sec. IV, we demonstrated that for positive values of D , sputter cones with selected slopes do not form if the initial surface protrusion is not sufficiently high and narrow. To illustrate this, we performed simulations of the generalized 1D EOM (33) with Gaussian initial conditions of the same height u_0 but with four different widths σ . Results from these simulations—which are shown in Fig. 12—reveal that selected slopes develop for the two smaller σ values but not for the larger two.

As is the case for $D = 0$, for positive values of D , a perturbation placed on the side of a cone moves away from the cone's tip and decreases in amplitude. If D is sufficiently large, then the perturbation smooths out almost entirely before it has moved down the side of the cone to an appreciable extent.

B. Simulations in 2D

The 2D EOM (7) was integrated numerically on the domain with $-L \leq x \leq L$ and $-L \leq y \leq L$ using the same method as we employed in 1D. Once again, periodic boundary conditions were applied. We set $L = 128$ and used an evenly spaced $N \times N$ grid with $N = 1024$ unless otherwise stated.

We begin by looking at the EOM (7) with $\gamma = 4$. In this case, we have the exact steady-state pyramidal solution given by Eq. (26) that is valid for all $\beta > -1$. Unless otherwise stated, simulations were carried out for $\beta = 0$. The initial condition used in these simulations was $u(x, y, 0) = u_0 \exp(-x^2/2\sigma_x^2 - y^2/2\sigma_y^2)$ with $u_0 = 420$ and $\sigma_x^2 = \sigma_y^2 = 1875$. Figure 13 shows that the surface evolves from the rotationally invariant Gaussian initial condition into a four-sided pyramid with rounded edges and a reduced height. The nearly pyramidal shape in Fig. 13(c) can be seen more clearly by looking at the surface contours shown in Fig. 13(d). Cross sections of the solid surface taken along the x and y axes (Fig. 14) along with the distribution of gradients for the entire surface (Fig. 15) agree very well with the analytical solution

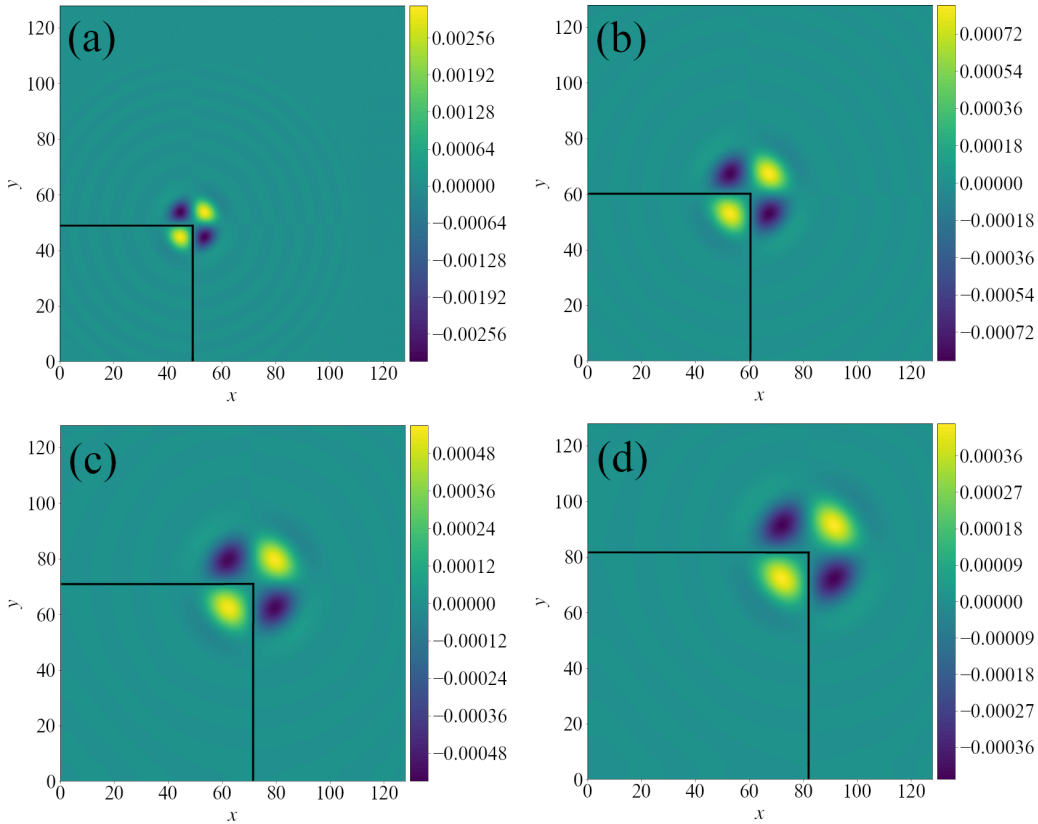


FIG. 17. A simulation of the EOM (7) with $\gamma = -2$ and $\beta = 0$. The initial condition was the exact pyramidal solution (22) with a Gaussian perturbation placed on the face located in the upper right quadrant of the x - y plane. The color scale represents the value of $u_{xy}(x, y, t)$ at (a) $t = 15$, (b) $t = 65$, (c) $t = 115$, and (d) $t = 165$. Only the region with $0 \leq x \leq L$ and $0 \leq y \leq L$ is shown in the figure. The black line segments intersect at the approximate center of the perturbation and are included to show that the disturbance is moving away from the cone's tip. As was the case in 1D, the perturbation broadens and decreases in amplitude as time passes.

(26) once the sputter cone has developed fully. In addition, Fig. 16 shows that, once the cone has formed, the results of the simulation agree closely with the constant recession velocity of the sputter cone that is predicted by Eq. (26). Finally, additional simulations showed that increasing β led to the formation of a pyramid with a more rounded tip and edges, with no change in the selected slopes, in accord with Eq. (26).

As was the case in 1D, starting the simulation with a different initial protrusion leads to the formation of a nearly identical cone provided that the initial protrusion's height is large enough compared to its width. If the initial protrusion does not satisfy this requirement, then four approximately parabolic regions form around the protrusion's tip. In this case, surface cuts taken along the x and y axes look very similar to those in the 1D simulations shown in Fig. 8.

In 2D, a small disturbance placed on one of the sides of the sputter cone propagates away from its apex, just as in 1D. To illustrate this, it is simplest to look at the case in which $\gamma = -2$ because the corresponding steady-state solution (22) has $u_{xy} = 0$ for all x, y , and t . Figure 17 shows the results of a simulation in which a Gaussian perturbation was placed on one face of the pyramidal sputter cone. $u_{xy}(x, y, t)$ has been plotted since it is small everywhere except in the immediate vicinity of the perturbation. As in 1D, the disturbance

broadens and decreases in amplitude as it propagates away from the sputter cone's tip.

Simulations of the rotationally invariant 2D EOM (7) with $\gamma = \beta = 0$ show that the surface tends towards a rotationally invariant cone regardless of the form of the initial protrusion, so long as the protrusion is sufficiently high and narrow. The results of two simulations with Gaussian initial conditions given by $u(x, y, 0) = u_0 \exp(-x^2/2\sigma_x^2 - y^2/2\sigma_y^2)$ are shown in Fig. 18. For the isotropic initial surface shown in Fig. 18(a), $\sigma_x^2 = \sigma_y^2 = 1875$, whereas $\sigma_x^2 = 2500$ and $\sigma_y^2 = 937.5$ for the anisotropic initial surface in Fig. 18(a'). In both cases, $u_0 = 500$. The corresponding surfaces at time $t = 1250$, which are shown in Figs. 18(b) and 18(b'), are close to being rotationally invariant, even though the initial condition in Fig. 18(a') is not. Cross sections of the solid surface taken along the x and y axes and the corresponding plots of the surface slope for the surface in Fig. 18(b) are shown in Fig. 19. The plots of u_x and u_y have regions of appreciable width on either side of the cone in which the slope is nearly constant. Additional evidence that the protrusion is close to being a rotationally invariant cone at sufficiently long times comes from the gradient distributions shown in Fig. 20. At any point on an idealized rotationally invariant cone except its apex, the slope $|\nabla u| = \sqrt{u_x^2 + u_y^2}$ has the same value. Thus, if we look at the gradient distribution in (u_x, u_y) space, then the highest slope counts should form

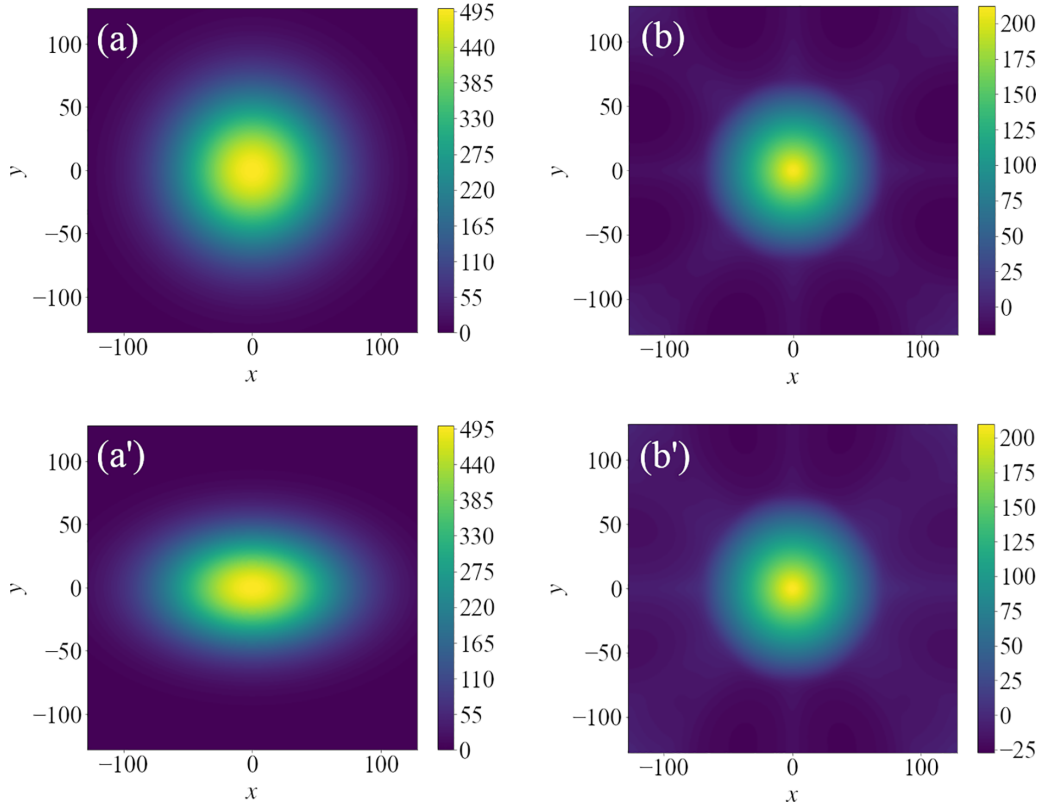


FIG. 18. Two simulations of Eq. (7) with $\beta = \gamma = 0$. The initial conditions are (a) a rotationally invariant Gaussian and (a') a Gaussian protrusion with differing widths σ_x and σ_y . The corresponding surfaces at time $t = 1250$ are shown in (b) and (b'), respectively. The false color ruler indicates the surface height $u(x, y, t)$.

a circle centered on the origin if the surface protrusion is nearly conical. Figure 20 shows that this indeed the case for

the surfaces shown in Figs. 18(b) and 18(b'), and so these protrusions have a nearly constant slope $|\nabla u|$ everywhere and not just along the Cartesian axes.

Let r and ϕ be polar coordinates for the x - y plane. If the surface protrusion is rotationally invariant, then u_ϕ is zero everywhere on it. To obtain more evidence that the surface tends toward being rotationally invariant regardless of the form of the initial protrusion, we computed the value of $Q \equiv \iint |u_\phi|^2 dx dy$ for a range of times for the simulation with the anisotropic initial condition shown in Fig. 18(a'). This integral was calculated for the domain within 256 grid points of the origin to eliminate the effect of the domain boundaries. The

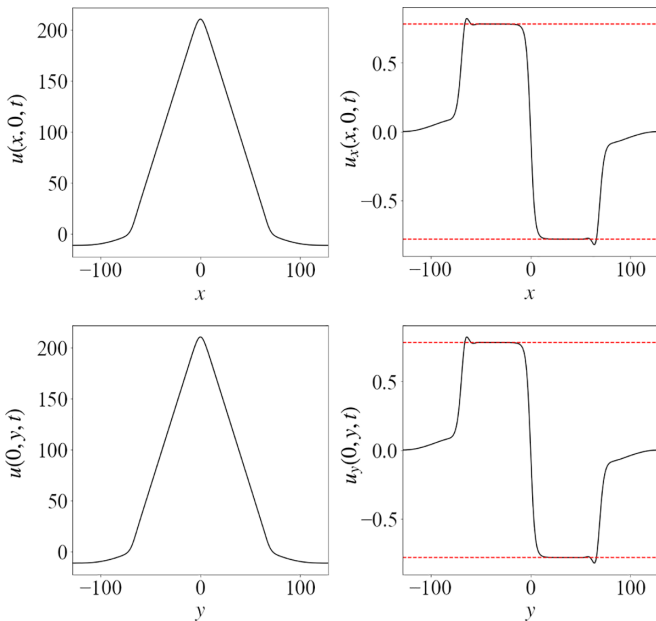


FIG. 19. Cross sections of the surface shown in Fig. 18(b) along the x - z and y - z planes together with the corresponding plots of the slopes u_x and u_y . The red dashed lines are located at $u_x = \pm 0.780$ and $u_y = \pm 0.780$, respectively.

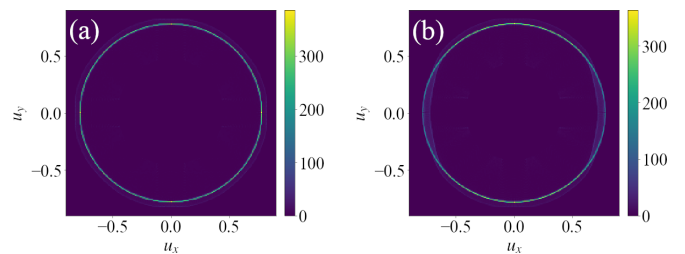


FIG. 20. The gradient distributions for the surfaces in Figs. 18(b) and 18(b') are shown in panels (a) and (b), respectively. The color scale represents the number of counts. Once again, values of the surface gradient near $(u_x, u_y) = (0, 0)$ were excluded since these come from the relatively flat region surrounding the cone.

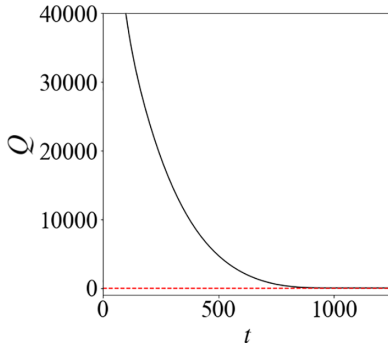


FIG. 21. A plot of Q versus time for the initial condition shown in Fig. 18(a').

plot of Q versus time shown in Fig. 21 shows that Q rapidly tends to zero as time passes, as expected.

Our simulations in 1D showed that the surface tends to the exact steady-state sputter cone solution provided that the initial protrusion is sufficiently high and narrow. We saw that this is also true for the 2D problem with $\gamma = 4$. In contrast, we were unable to find an exact sputter cone solution for the rotationally invariant 2D EOM with $\gamma = \beta = 0$. However, our simulations of this EOM do provide strong evidence that the surface tends to a rotationally invariant steady-state sputter cone regardless of the form of the initial protrusion, so long as the protrusion is sufficiently high and narrow. This is illustrated by Fig. 22. The near perfect agreement of the plots in the vicinity of the cone's tip show that a steady state was reached. Moreover, as in the other cases we have considered, the velocity of the cone's tip $u_t(0, 0, t)$ was found to be very nearly constant after the cone had fully formed, as seen in Fig. 23. The value of the steady-state recession velocity $v_0 \cong 0.238$ was obtained by averaging many values of $u_t(0, 0, t)$ within the time interval in which it is approximately constant. A value for v_0 can also be obtained by inserting the value of

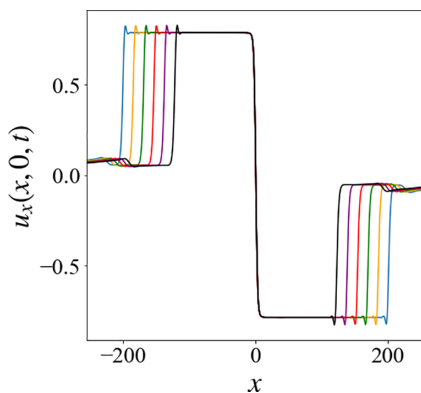


FIG. 22. Six snapshots of $u_x(x, 0, t)$ taken during the time period in which the fully formed sputter cone is receding into the surface. The blue and black curves were taken at times $t = 1500$ and $t = 1750$, respectively, while the intervening snapshots were taken at time intervals of $\Delta t = 50$. The initial surface for this simulation was given by $u(x, y, 0) = u_0 \exp(-x^2/2\sigma_x^2 - y^2/2\sigma_y^2)$ with $u_0 = 500$ and $\sigma_x^2 = \sigma_y^2 = 7500$. The simulation domain was the region in which $-512 \leq x \leq 512$ and $-512 \leq y \leq 512$.

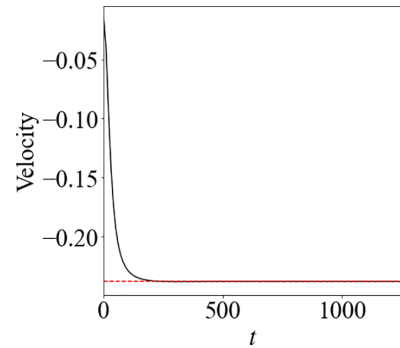


FIG. 23. The recession velocity $u_t(0, 0, t)$ of the cone's tip versus time for the initial condition shown in Fig. 18(a). The red dashed line is located at the velocity $-v_0 = -0.238$.

the cone's slope s we found in Fig. 19 into Eq. (31). This yields $v_0 \cong 0.238$, in agreement with the value we obtained directly.

To study the behavior of a small disturbance to the form of the rotationally invariant cone, we started a simulation with an initial condition of the form $u(x, y, 0) = -sr$, which represents a cone with a pointed tip. The value of s was chosen to be the numerically determined approximate slope of our simulated cones, $s = 0.780$. The simulated surface evolved into a steady-state cone with a rounded tip very quickly relative to the simulations beginning with a Gaussian. Perturbations placed on the sputter cone propagate away from the cone's tip, in analogy with the behavior of the sputter cones studied earlier. This is illustrated by Fig. 24. In this simulation, a sinusoidal perturbation that depends only on r was superimposed on the sputter cone. The ripples propagate radially outward, away from the cone's tip, until the constant slope regions are restored. The ripples also attenuate with time.

VI. DISCUSSION

We began this paper by studying the surface dynamics of the ion-bombarded surface for the 1D case in which the surface height h does not depend on y . At this point in our work, we only included the effects of sputtering and a fourth-order smoothing term in our analysis. This problem has also been studied by Holmes-Cerfon *et al.* [29,30] for an empirical form of $Y(b)$ with the values of two parameters chosen to model 1-keV Ar^+ bombardment of a silicon surface. Their numerical work suggests that if a sufficiently high and narrow ridge is initially present on the surface of the sample, then the ridge will evolve into a so-called knife edge with sides of a particular selected slope. This knife edge is analogous to the 1D sputter cone we found for our choice of yield function; both are doubly undercompressive shocks.

Holmes-Cerfon *et al.* were forced to determine the form of their knife edge numerically. In contrast, the 1D sputter cone solution we found for the simple, generic yield function given by Eq. (11) is exact. The yield function we elected to study also leads to the parameter-free EOM (9) and so we did not need to choose parameter values to model a particular ion-target combination. Instead, the parameters in our model were simply scaled away. The values of these parameters determine

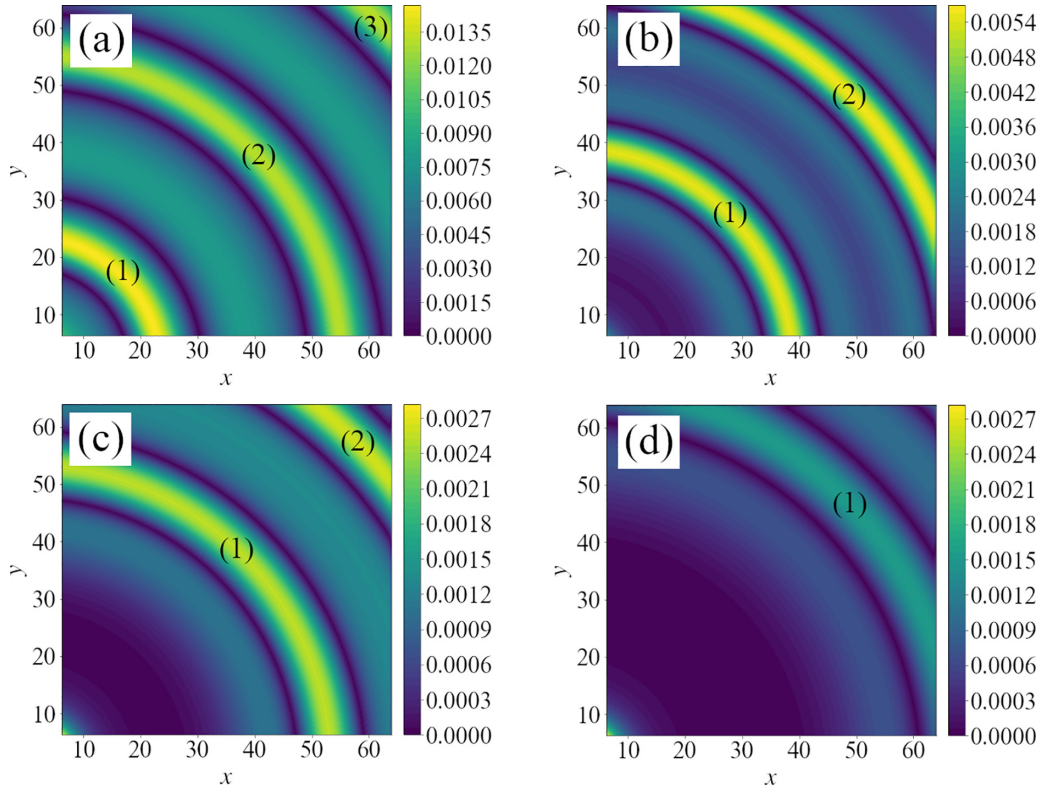


FIG. 24. A simulation of the EOM (7) with $\gamma = \beta = 0$ starting with the initial condition described in the text. The color scale represents the value of $|u_{rr}|$ at (a) $t = 5$, (b) $t = 150$, (c) $t = 300$, and (d) $t = 450$. Over time, the ripples that were superimposed on the sputter cone move away from the cone's tip, which is located at the origin. The labels (1)–(3) track the individual ripples as time passes. The ripples also attenuate with the passage of time. Note that only the region with $6 \leq x \leq 64$ and $6 \leq y \leq 64$ is shown, but the simulation was carried out the domain with $-128 \leq x \leq 128$ and $-128 \leq y \leq 128$.

the characteristic time scale and the characteristic horizontal and vertical length scales.

Holmes-Cerfon *et al.* omitted terms proportional to second-order spatial derivatives of the surface height from their EOM. They did so even though the effects of curvature-dependent sputtering and mass redistribution can be substantial if the target material is amorphized by the ion irradiation. Similarly, if the material remains crystalline, then the Ehrlich-Schwoebel effect can lead to the presence of a non-negligible term proportional to u_{xx} in the EOM. In our work, we studied the effect of adding a term Du_{xx} to the 1D EOM. We found that a sputter cone solution exists for D smaller than the critical value D_c but not for $D > D_c$.

The undercompressive shocks studied in this paper and by Holmes-Cerfon *et al.* [29,30] are doubly undercompressive. In an earlier study, Chen and coworkers [28] found that singly undercompressive shocks can form when a pit in an otherwise flat solid surface is irradiated with a broad, normally incident ion beam. In addition, when a solid surface is bombarded with a broad ion beam at an angle of ion incidence θ that exceeds a critical value, surface ripples develop. If θ is sufficiently large, then the surface often develops a terraced form at long times. A theory for terrace formation has been advanced in which the terraces are singly undercompressive shocks [39,40].

Undercompressive shocks appear in other contexts besides ion bombardment of solid surfaces. They can occur, for example, when a fluid thin film flows down an inclined plane

subject to the competing effects of gravity and a thermal gradient. The EOM for that problem is

$$h_t + \partial_x(h^2 - h^3) = -\partial_x(h^3 h_{xxx}) + D\partial_x(h^3 h_x), \quad (47)$$

where $h = h(x, t)$ is the film thickness and the non-negative, dimensionless parameter D is a measure of the relative strength of the gravitational, viscous, and surface tension forces [41]. Equation (47) has a number of features in common with the generalized 1D EOM we studied in Sec. IV, Eq. (33). Differentiating the latter with respect to x yields

$$b_t + \partial_x(b^2 - b^4) = -b_{xxxx} + Db_{xx}, \quad (48)$$

where, as before, $b \equiv u_x$. Although Eqs. (47) and (48) have different fluxes, both fluxes are nonconvex functions. Both equations also have second-order and fourth-order smoothing terms. Equation (48) is the simpler of the two, however, because the smoothing terms are linear in this case but not in the case of Eq. (47).

In the thin film flow problem, Bertozzi and coworkers were able to prove that an undercompressive shock exists for sufficiently small, non-negative D and that one does not exist when D is sufficiently large [41]. The proof was a mathematical *tour de force*. In contrast, for the model of sputter cone formation given by Eq. (48), we were able to demonstrate that an undercompressive shock exists for $D < D_c = 6^{1/3}$ by explicitly and analytically finding the form of the shock. No

such solution exists for $D \geq D_c$, and so we have found the exact critical value of D for our problem.

In the 2D case, the surface height h has a nontrivial dependence on both x and y . This is the case that is directly relevant to experiments on sputter cone formation. In our theory, a sputter cone is a generalization of a doubly undercompressive shock to 2D. Our 2D EOM (7) can be separated into two 1D problems for $\gamma = -2$ and $\gamma = 4$. For these special cases, a sputter cone is a square pyramid that is obtained by the superposition of two orthogonal 1D doubly undercompressive shocks. The isotropic 2D case in which $\beta = \gamma = 0$ cannot be separated into two 1D problems. Nevertheless, our numerical work showed that sputter cones form in this case as well. These sputter cones are rotationally invariant steady-state solutions to the EOM.

In early work on sputter cones, Stewart and Thompson argued that the flanks of the cones have a slope that maximizes the rate that the surface recedes [42]. In the case of our model, the sputter yield (11) takes on its greatest value for the (dimensionless) slope $1/\sqrt{2} \cong 0.707$. This is quite different than the slope of the sides of the cone $s = 0.780$ that we found for the isotropic case in 2D. The simple argument given by Stewart and Thompson gives the incorrect result because the effect of the fourth-order smoothing term was neglected. As we have seen, this term comes from either surface diffusion or ion-induced viscous flow in a surface layer and its effect must be taken into account if sputter cones are to form. Others have suggested that the redeposition of sputtered material is essential to the formation of sputter cones, and that the cones actually grow in the direction of the incident ions [43]. Our work shows that sputter cones can develop in the absence of redeposition. Our sputter cones also move downward, away from the ion source.

In both 1D and 2D, a wide variety of initial conditions evolve into sputter cones as time passes; our simulations suggest that so long as an initial protrusion is sufficiently high and narrow, it converges to a sputter cone with the passage of time. Away from the apex, the slope of the sputter cone takes on a single selected value. The cone opening angle can therefore take on only one value, in accord with experiment [1–8]. In our simulations, sputter cones appear to be stable against perturbations—a disturbance to the form of a cone propagates away from the cone apex, and decreases in amplitude as it does so. This is consistent with experiment, since sputter cones would not be observed experimentally if they were not stable.

Consider the isotropic case in which $\gamma = \beta = 0$. We set $\tilde{h} = (C/B)^{1/3}h$ and $\tilde{Y}_0 = cY_0/a^2$ and define \tilde{x} , \tilde{y} and \tilde{t} as previously. After dropping the tildes, our EOM (5) becomes

$$h_t = -Y - \nabla^2 \nabla^2 h, \quad (49)$$

where the rescaled sputter yield Y is given by

$$Y = Y_0 + (\nabla h)^2 - (\nabla h)^4. \quad (50)$$

As we have already discussed, this sputter yield has a number of desirable features. It becomes negative for sufficiently large slopes $|\nabla h|$, however. To address this issue, we consider the

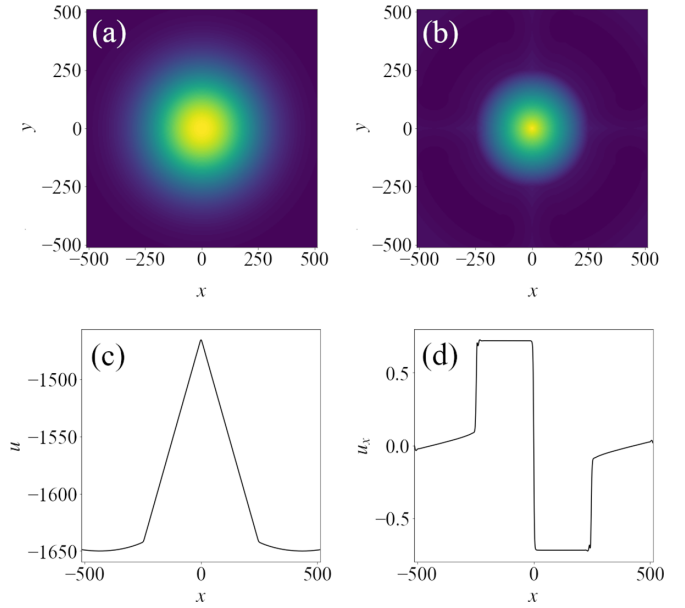


FIG. 25. A numerical integration of the EOM (49) with Y replaced by the modified sputter yield Y_m and with Y_0 set to 1. The domain is the region with $-512 \leq x \leq 512$ and $-512 \leq y \leq 512$. (a) The Gaussian initial condition $u(x, y, 0) = u_0 \exp(-x^2/2\sigma_x^2 - y^2/2\sigma_y^2)$ with $u_0 = 500$ and $\sigma_x^2 = \sigma_y^2 = 7500$. (b) The surface at time $t = 1650$. (c) The cross section of the surface shown in (b) along the x - z plane. (d) The corresponding plot of the slope u_x .

modified sputter yield

$$Y_m = \frac{Y_0 + (\nabla h)^2}{Y_0 + (\nabla h)^4}. \quad (51)$$

This modified yield, like the original yield given by Eq. (50), at first increases with the slope $|\nabla h|$ before reaching a maximum and then it decreases monotonically. Y_m , however, does not become negative for large slopes. Instead, it tends to zero as $|\nabla h|$ becomes large, as it should. In addition, for small slopes $|\nabla h|$, Y_m reduces to Y to order $(\nabla h)^4$.

We carried out numerical integrations of the EOM (49) with Y replaced by the modified sputter yield Y_m . Figure 25 shows the results of a simulation with a rotationally invariant Gaussian protrusion as the initial condition. Once again, the initial protrusion evolves into a cone with a rounded tip. This suggests that the main results we have obtained in this paper do not depend on the detailed form of the sputter yield, i.e., that they are robust.

The reader might reasonably ask why we did not use the modified yield Y_m throughout our work. The answer to this question is that by choosing the sputter yield given by Eq. (50) we were able to obtain analytical results in 1D and in the separable 2D problems.

VII. CONCLUSIONS

In this paper, we advanced a simple model that leads to sputter cone formation. We showed that the model need only include the angular dependence of the sputter yield and a fourth-order smoothing effect like surface diffusion for sputter cones to form. We began by studying our model in 1D. We

found that a sputter cone is a particular kind of shock wave that is known as a doubly undercompressive shock. Our simulations showed that a sputter cone is formed provided that the initial surface protrusion is sufficiently tall and narrow, and that the opening angle of the cone does not depend on the detailed form of the initial condition. A small disturbance on the side of the sputter cone attenuates as it propagates away from the cone's apex, and hence the cone is stable against perturbations.

We also studied a generalized version of the 1D model that includes a term proportional to the second-order spatial derivative of the surface height. Such a term could come from curvature-dependent sputtering or ion-induced mass redistribution, for example. This generalized model produces sputter cones so long as the coefficient of the second-order term does not exceed a critical value.

In 2D, a sputter cone is a higher-dimensional analog of a doubly undercompressive shock. There are two particularly simple special cases in which the crystal structure has four-fold rotational symmetry. For these cases, a sputter cone is a four-sided pyramid with rounded edges that is produced by the superposition of two orthogonal, one-dimensional, doubly undercompressive shocks. If the target material is amorphous, then a sputter cone is a rotationally invariant cone with a rounded tip. In this case, we were unable to find the form of the sputter cone analytically, but our numerical work strongly suggests that a steady-state form is approached that has a

form that is independent of the detailed form of the initial protrusion, so long as the protrusion is sufficiently high and narrow. In all cases, a small disturbance to the form of the sputter cone attenuates in amplitude as it propagates away from the cone's tip. A sputter cone is eventually eroded away in both one and two dimensions.

We adopted a particularly simple form for the sputter yield's dependence on the angle of ion incidence. This allowed to find the form of the sputter cone analytically in 1D and in the two simple special cases in 2D. However, simulations carried out with a modified sputter yield strongly suggest that our main conclusions are valid for any physically reasonable choice of sputter yield.

For the sake of simplicity, in this paper we studied the sputter cones that are formed by bombarding a target that consists of a thin film of a low sputter yield material **A** that has been deposited on the planar surface of a high sputter yield bulk material **B**. Sputter cones are usually produced by bombarding the initially planar surface of a solid composed of the material **B** while concurrently depositing atoms of species **A**, however. In future work, we plan to develop a theory for this more challenging problem.

ACKNOWLEDGMENT

This work was supported by Grant No. DMR-2116753 awarded by the U.S. National Science Foundation.

-
- [1] G. K. Wehner and D. J. Hajicek, *J. Appl. Phys.* **42**, 1145 (1971).
 - [2] S. M. Rossnagel and R. S. Robinson, *Radiat. Eff.* **58**, 11 (1981).
 - [3] R. S. Robinson and S. M. Rossnagel, *J. Vac. Sci. Technol.* **21**, 790 (1982).
 - [4] S. Morishita and F. Okuyama, *J. Vac. Sci. Technol. A* **8**, 3295 (1990).
 - [5] Y. Mori, Y. Fujimoto, and F. Okuyama, *Nucl. Instrum. Methods B* **63**, 395 (1992).
 - [6] G. Shang, F. Y. Meng, F. C. K. Au, Q. Li, C. S. Lee, I. Bello, and S. T. Lee, *Adv. Mater.* **14**, 1308 (2002).
 - [7] N. G. Shang, X. L. Ma, C. P. Liu, I. Bello, and S. T. Lee, *Phys. Status Solidi A* **207**, 309 (2010).
 - [8] S.-C. Song, Y. Qiu, H.-C. Hao, and M. Lu, *Appl. Phys. A* **119**, 1033 (2015).
 - [9] A. Güntherschulze and W. Tollmien, *Z. Phys.* **119**, 685 (1942).
 - [10] R. Reiche and W. Hauffe, *Appl. Surf. Sci.* **165**, 279 (2000).
 - [11] M. Otto, M. Algasinger, H. Branz, B. Gesemann, T. Gimpel, K. Füchsel, T. Käsebier, S. Kontermann, S. Koynov, X. Li *et al.*, *Adv. Opt. Mater.* **3**, 147 (2015).
 - [12] V. B. Shenoy, W. L. Chan, and E. Chason, *Phys. Rev. Lett.* **98**, 256101 (2007).
 - [13] R. M. Bradley and P. D. Shipman, *Phys. Rev. Lett.* **105**, 145501 (2010).
 - [14] P. D. Shipman and R. M. Bradley, *Phys. Rev. B* **84**, 085420 (2011).
 - [15] J. Zhou and M. Lu, *Phys. Rev. B* **82**, 125404 (2010).
 - [16] R. M. Bradley, *Phys. Rev. B* **83**, 195410 (2011).
 - [17] R. M. Bradley and P. D. Shipman, *Appl. Surf. Sci.* **258**, 4161 (2012).
 - [18] R. M. Bradley, *Phys. Rev. B* **85**, 115419 (2012).
 - [19] R. M. Bradley, *Phys. Rev. B* **87**, 205408 (2013).
 - [20] R. M. Bradley, *J. Appl. Phys.* **119**, 134305 (2016).
 - [21] The effect that implantation of nonvolatile ions has on the surface dynamics is studied in R. M. Bradley and H. Hofsäss, *J. Appl. Phys.* **120**, 074302 (2016); H. Hofsäss, K. Zhang, and O. Bobes, *ibid.* **120**, 135308 (2016).
 - [22] C. C. Umbach, R. L. Headrick, and K.-C. Chang, *Phys. Rev. Lett.* **87**, 246104 (2001).
 - [23] P. Sigmund, *J. Mater. Sci.* **8**, 1545 (1973).
 - [24] R. M. Bradley and J. M. E. Harper, *J. Vac. Sci. Technol. A* **6**, 2390 (1988).
 - [25] G. Carter and V. Vishnyakov, *Phys. Rev. B* **54**, 17647 (1996).
 - [26] M. Moseler, P. Gumbsch, C. Casiraghi, A. C. Ferrari, and J. Robertson, *Science* **309**, 1545 (2005).
 - [27] B. Davidovitch, M. J. Aziz, and M. P. Brenner, *Phys. Rev. B* **76**, 205420 (2007).
 - [28] H. H. Chen, O. A. Urquidez, S. Ichim, L. H. Rodriguez, M. P. Brenner, and M. J. Aziz, *Science* **310**, 294 (2005).
 - [29] M. Holmes-Cerfon, W. Zhou, A. L. Bertozzi, M. P. Brenner, and M. J. Aziz, *Appl. Phys. Lett.* **101**, 143109 (2012).
 - [30] M. Holmes-Cerfon, M. J. Aziz, and M. P. Brenner, *Phys. Rev. B* **85**, 165441 (2012).
 - [31] G. B. Whitham, *Linear and Nonlinear Waves* (Wiley, New York, 1974).
 - [32] U. Valbusa, C. Boragno, and F. B. De Mongeot, *J. Phys.: Condens. Matter* **14**, 8153 (2002).
 - [33] A. Levandovsky and L. Golubović, *Phys. Rev. B* **69**, 241402(R) (2004).

- [34] E. Chason and W. L. Chan, Spontaneous patterning of surfaces by low-energy ion beams, in *Materials Science with Ion Beams*, Topics in Applied Physics Vol. 116, edited by H. Bernas (Springer, Berlin, Heidelberg, 2010).
- [35] L. Golubović, A. Levandovsky, and D. Moldovan, *East Asian J. Appl. Math.* **1**, 297 (2011).
- [36] A. L. Bertozzi, A. Münch, X. Fanton, and A. M. Cazabat, *Phys. Rev. Lett.* **81**, 5169 (1998).
- [37] A. L. Bertozzi, A. Münch, and M. Shearer, *Physica D* **134**, 431 (1999).
- [38] S. M. Cox and P. C. Matthews, *J. Comput. Phys.* **176**, 430 (2002).
- [39] D. A. Pearson and R. M. Bradley, *J. Phys.: Condens. Matter* **27**, 015010 (2015).
- [40] M. P. Harrison, D. A. Pearson, and R. M. Bradley, *Phys. Rev. E* **96**, 032804 (2017).
- [41] A. L. Bertozzi and M. Shearer, *SIAM J. Math. Anal.* **32**, 194 (2000).
- [42] A. Stewart and M. Thompson, *J. Mater. Sci.* **4**, 56 (1969).
- [43] G. Wehner, *Appl. Phys. Lett.* **43**, 366 (1983).